k-Space Image Correlation Spectroscopy: A Method for Accurate Transport Measurements Independent of Fluorophore Photophysics

David L. Kolin,* David Ronis,*† and Paul W. Wiseman*†
*Department of Chemistry, and †Department of Physics, McGill University, Montreal, Quebec, H3A 2K6, Canada

ABSTRACT We present the theory and application of reciprocal space image correlation spectroscopy (kICS). This technique measures the number density, diffusion coefficient, and velocity of fluorescently labeled macromolecules in a cell membrane imaged on a confocal, two-photon, or total internal reflection fluorescence microscope. In contrast to r-space correlation techniques, we show kICS can recover accurate dynamics even in the presence of complex fluorophore photobleaching and/or "blinking". Furthermore, these quantities can be calculated without nonlinear curve fitting, or any knowledge of the beam radius of the exciting laser. The number densities calculated by kICS are less sensitive to spatial inhomogeneity of the fluorophore distribution than densities measured using image correlation spectroscopy. We use simulations as a proof-of-principle to show that number densities and transport coefficients can be extracted using this technique. We present calibration measurements with fluorescent microspheres imaged on a confocal microscope, which recover Stokes-Einstein diffusion coefficients, and flow velocities that agree with single particle tracking measurements. We also show the application of kICS to measurements of the transport dynamics of α5-integrin/enhanced green fluorescent protein constructs in a transfected CHO cell imaged on a total internal reflection fluorescence microscope using charge-coupled device area detection.

INTRODUCTION

Studies of the dynamics of a membrane protein can yield important information regarding its biological functions (1). Several techniques have been developed to quantify the dynamics of fluorescently tagged proteins, including fluorescence correlation spectroscopy (FCS) (2), temporal image correlation spectroscopy (TICS) (3), fluorescence recovery after photobleaching (FRAP) (4), and single particle tracking (SPT) (5).

The recent development of green fluorescent protein (GFP), and its variants such as CFP, YFP, and citrine, have revolutionized the field of cellular biophysics by allowing unprecedented convenience and specificity of labeling in living cells (6). However, these fusion proteins are known to both irreversibly and/or reversibly photobleach on a variety of timescales (7,8). Recently, quantum dots (QDs) have been proposed as a potential replacement for organic fluorophores, because they are bright, have wide excitation and narrow emission spectra, and are resistant to photobleaching (9,10). Although photobleaching is less of an issue for QDs, they do exhibit nonstationary intermittent fluorescence emission (''blinking'') (11), which complicates FCS or TICS studies (12) and limits the acquisition time of SPT trajectories. The bleaching and blinking of organic dyes and QDs can complicate the quantitative analysis of dynamics or make an accurate determination impossible (13). In addition, because QDs are difficult to photobleach, they cannot be used in FRAP studies.

The number densities and aggregation states of membrane proteins, especially receptors, are closely linked to their signaling and activation states (14). Spatial image correlation spectroscopy (ICS) has been developed as a technique that can measure the density and aggregation state of fluorescently labeled membrane proteins (15,16). However, ICS requires a random and relatively uniform distribution of particles, a requirement that is sometimes not met in spatially heterogeneous biological membranes such as neurons.

Recently, two variants of FCS have emerged: FCS with traveling interference fringe excitation (FCSTFE) (17) and Fourier imaging correlation spectroscopy (FICS) (18,19). These k-space fluorescence correlation techniques can measure the structure factor and dynamics of fluorescently labeled particles by probing selective spatial frequencies using an interference pattern generated from two lasers. They have been applied to study solutions of dyes (20) and polystyrene spheres (17), and the mitochrondrial riticulum (19).

In this work, we present a novel technique for measuring dynamics and number densities of fluorescently tagged membrane proteins: k-space image correlation spectroscopy (kICS). We will show that this method complements other techniques by providing distinct advantages over its r-space correlation counterparts. Its chief benefits are: the recovery of transport coefficients that are completely insensitive to systematic errors from fluorophore blinking, and reversible and irreversible bleaching; it does not require measurement of the point spread function (PSF) of the imaging system; nonlinear curve fitting is not required for the analysis of one population; and, it can detect the velocity of flowing proteins in the presence of a diffusing population.

We begin by deriving the theoretical form of a reciprocal-space time correlation function for a sample of fluorescent particles undergoing diffusion and flow, as imaged using a laser scanning microscope (LSM) or total internal reflection

Submitted February 13, 2006, and accepted for publication June 21, 2006.

Address reprint requests to Paul W. Wiseman, E-mail: paul.wiseman@mcgill.ca.

0006-3495/06/10/3061/15 $2.00 doi: 10.1529/biophysj.106.082768

fluorescence microscope (TIRFM). We analyze image series of diffusing and flowing fluorescent microspheres as a proof-of-principle, in which we recover Stokes-Einstein diffusion coefficients, and particle velocities. We present simulations that show that kICS can recover accurate diffusion coefficients and velocities even in the presence of complex fluorophore photobleaching and blinking photophysics. We show that absolutely no knowledge of the fluorophore photophysics is necessary to extract accurate results. Finally, we apply the method to living cells to measure protein transport, by imaging and analyzing the basal membrane of a living CHO cell transfected with α5-integrin/eGFP on a TIRFM using area detection with a charge-coupled device (CCD) camera.

THEORY

The kICS technique involves correlating, in time, the spatial Fourier transforms of individual images in an image time series. We will begin by deriving the form of the Fourier transform of a single image in terms of particle positions and the instrumental PSF. We will then show how, by correlating these two-dimensional (2D) Fourier transforms, information regarding the dynamics and number densities of the sample can be extracted. Both heterodyne light scattering (21) and the kICS method probe particle-particle correlations. Although these techniques vary widely in their experimental setup, data analysis, and the systems typically studied, the underlying theory is very similar.

An image series of fluorescence intensities collected on a LSM or TIRFM, $i(\mathbf{r}, t)$, is a convolution of the microscopic number density, ρ $(\mathbf{r}, t)$, and the instrumental point spread function (PSF), $I(\mathbf{r})$:

$$i(\mathbf{r}, t) = qI(\mathbf{r}) * \rho(\mathbf{r}, t), \tag{1}$$

where q is a constant that includes the quantum yield of the fluorophore, the collection efficiency, and the detector gain. We will begin by assuming a 2D system is being imaged, and later extend the theory to three-dimensional (3D) systems. The microscopic number density of fluorescing particles at point $\mathbf{r}$ and time t is given by:

$$\rho(\mathbf{r}, t) \equiv \sum_{i=1}^{N} \Theta_i(t)\delta(\mathbf{r} - \mathbf{r}_i(t)), \tag{2}$$

where the sum is over all N particles in the system, δ is the Dirac δ-function, and $\mathbf{r}_i(t)$ is the position of the i^{th} particle at time t. The sum is only over those particles that are emitting due to the factor $\Theta_i(t)$:

$$\Theta_i(t) = \begin{cases} 1 & \text{if } i \text{ is fluorescing at time } t \\ 0 & \text{otherwise.} \end{cases} \tag{3}$$

This change in fluorescence could be due to fluorophore photobleaching, or blinking. Assuming a 2D sample is being imaged, the PSF of a confocal or two-photon LSM is modeled as a 2D Gaussian (TEM_{00}), and for a TIRFM it is an Airy disk that can be approximated as a 2D Gaussian:

$$I(\mathbf{r}) = I_0 \exp\left[-2\left(\frac{x^2 + y^2}{\omega_0^2}\right)\right], \tag{4}$$

where I_0 is the laser intensity at the center of the focus, and ω_0 is the e^{-2} beam radius of the laser beam in the lateral direction.

We will now express the 2D spatial Fourier transform of an image, $\tilde{i}(\mathbf{k}, t)$ as a function of $\rho(t, \mathbf{r})$ and $I(\mathbf{r})$. Because the image recorded is a convolution of these two functions, $\tilde{i}(\mathbf{k}, t)$ is simply the product of the spatial Fourier transforms of each function:

$$\tilde{i}(\mathbf{k}, t) = q\tilde{I}(\mathbf{k})\tilde{\rho}(\mathbf{k}, t), \tag{5}$$

where $\tilde{f}(k)$ is the Fourier transform of function $f(x)$ for variable x. In general, we use the Fourier transform convention $\tilde{f}(\mathbf{k}) \equiv \int d\mathbf{r} \exp(i\mathbf{k} \cdot \mathbf{r}) f(\mathbf{r})$. The 2D spatial Fourier transform of the excitation profile (Eq. 4), $\tilde{I}(\mathbf{k})$, is

$$\tilde{I}(\mathbf{k}) = \frac{I_0\omega_0^2\pi}{2} \exp\left[-\frac{\omega_0^2|\mathbf{k}|^2}{8}\right], \tag{6}$$

and is often called the optical transfer function. The spatial Fourier transform of $\rho(\mathbf{r}, t)$ (Eq. 2), is:

$$\tilde{\rho}(\mathbf{k}, t) = \sum_{i=1}^{N} \Theta_i(t) \exp[i\mathbf{k} \cdot \mathbf{r}_i(t)]. \tag{7}$$

By substituting Eqs. 6 and 7 into Eq. 5, we find an expression for the reciprocal space image, in terms of the particle positions and the PSF, namely

$$\tilde{i}(\mathbf{k}, t) = \frac{qI_0\omega_0^2\pi}{2} \sum_{i=1}^{N} \Theta_i(t) \exp\left[i\mathbf{k} \cdot \mathbf{r}_i(t) - \frac{\omega_0^2|\mathbf{k}|^2}{8}\right]. \tag{8}$$

Next we define a reciprocal-space time correlation function, $r(\mathbf{k}, \tau)$, as:

$$r(\mathbf{k}; \tau, t) = \langle \tilde{i}(\mathbf{k}, t)\tilde{i}^*(\mathbf{k}, t + \tau) \rangle, \tag{9}$$

where the angular brackets denote a time average. The notation $\tilde{i}^*(\mathbf{k}, t+\tau)$ denotes the complex conjugate of the 2D spatial Fourier transform of image $i(\mathbf{r}, t + \tau)$. Because the experimentally collected image series is discrete in both space and time, Eq. 9 is calculated as follows:

$$r(\mathbf{k}; s, c) = \frac{1}{P - s} \sum_{c=0}^{P-s-1} \tilde{i}(\mathbf{k}, c)\tilde{i}^*(\mathbf{k}; c + s), \tag{10}$$

where P is the total number of images, s is the temporal lag variable evaluated from 0 to $P - 1$, and where the result won't depend on c if the system is stationary on average.

By expressing $r(\mathbf{k};\tau, t)$, Eq. 9, in terms of the Fourier transform of an image, Eq. 8, yields:

$$r(\mathbf{k}; \tau, t) = \frac{q^2 I_0^2 \omega_0^4 \pi^2}{4} \times \left\langle \sum_{i=1}^{N} \Theta_i(t) e^{i\mathbf{k}\cdot\mathbf{r}_i(t) - \frac{\omega_0^2|\mathbf{k}|^2}{8}} \sum_{j=1}^{N} \Theta_j(t)(\tau) e^{-i\mathbf{k}\cdot\mathbf{r}_j(t+\tau) - \frac{\omega_0^2|\mathbf{k}|^2}{8}} \right\rangle. \tag{11}$$

If we assume that the system is sufficiently dilute such that the particles are independent, and thus only correlate with themselves, the cross-product terms $\langle e^{i\mathbf{k}\cdot\mathbf{r}_i(t)}e^{-i\mathbf{k}\cdot\mathbf{r}_j(t+\tau)}\rangle = 0$ for $i \neq j$. Strictly speaking, these terms will be proportional to an extra factor of the fluorophore concentration and will be small for dilute systems (21). Consequently, we can omit these, drop the i and j subscripts, and only sum once over the total number of particles. Furthermore, if we assume the fluorescence emission function $\Theta_i(t)$ is independent of other dynamic processes, and the particles are identical, Eq. 11 becomes

$$r(\mathbf{k};\tau,t) = N\frac{q^2I_0^2\omega_0^4\pi^2}{4}\langle\Theta(t)\Theta(t+\tau)\rangle \times \left\langle \exp\left[i\mathbf{k}\cdot(\mathbf{r}(t)-\mathbf{r}(t+\tau)) - \frac{\omega_0^2|\mathbf{k}|^2}{4}\right]\right\rangle. \quad (12)$$

For systems with one population, undergoing either diffusion, flow, or diffusive flow (i.e., diffusion with drift), Eq. 12 becomes ((22–24); also sections 5.4 and 5.8 of Berne and Pecora (21)),

$$r(\mathbf{k};\tau,t) = N\frac{q^2I_0^2\omega_0^4\pi^2}{4}\langle\Theta(t)\Theta(t+\tau)\rangle \times \exp\left[i\mathbf{k}\cdot\mathbf{v}\tau - |\mathbf{k}|^2\left(D\tau+\frac{\omega_0^2}{4}\right)\right], \quad (13)$$

where D is the diffusion coefficient, and $\mathbf{v}$ is the velocity of the fluorescent particles. Note that t won't drop out if the optical processes are nonstationary, e.g., as would be the case where photobleaching is occurring.

3D diffusion

We will now extend the theory to 3D systems. As with the 2D systems, a 2D Fourier transform is performed on the images. However, because the images are sampled from the same x-y plane in the axial (z) direction, no Fourier transform is performed in the third dimension. Consequently, the analytical form of the k-space time correlation function obtained from a 3D sample imaged as $i(\mathbf{r}|_{z=\text{constant}}, t)$ on a LSM is of the form $r(\mathbf{k}_\parallel, z;\tau, t)$, where, henceforth, we use the subscript $\parallel$ to denote the projection of the subscripted vector on the x-y plane. As before, we assume that the PSF for a LSM in the axial direction can be approximated by a Gaussian:

$$I(\mathbf{r}) = I_0\exp\left[-2\left(\frac{\mathbf{r}_\parallel^2}{\omega_0^2}+\frac{z^2}{z_0^2}\right)\right], \quad (14)$$

where z_0 is the e^{-2} beam radius in the axial direction. In this case, the analytical form of $r(\mathbf{k}_\parallel, z, \tau)$ for a 3D sample is given by inverse Fourier transforming Eq. 9 with respect to k_z:

$$\langle\tilde{i}(\mathbf{k}_\parallel,z;t)\tilde{i}^*(\mathbf{k}_\parallel,z;t+\tau)\rangle = \int_{-\infty}^{\infty}\int_{-\infty}^{\infty}\frac{dk_z\,dk_z'}{(2\pi)^2}e^{i(k_zz-k_z'z)}[q\tilde{I}(\mathbf{k})]^2 \times\langle\tilde{\boldsymbol{\rho}}(\mathbf{k},t)\tilde{\boldsymbol{\rho}}^*(\mathbf{k}',t+\tau)\rangle. \quad (15)$$

By separating $\mathbf{k}$ into $\mathbf{k}_\parallel$ and k_z, and using Eqs. 12 and 13 we find:

$$\langle\tilde{i}(\mathbf{k}_\parallel,z;t)\tilde{i}^*(\mathbf{k}_\parallel,z;t+\tau)\rangle = N\frac{q^2I_0^2\omega_0^4z_0^2\pi^3}{8}\langle\Theta(t)\Theta(t+\tau)\rangle\exp\left[i\mathbf{k}_\parallel\cdot\mathbf{v}_\parallel\tau - |\mathbf{k}_\parallel|^2\left(D\tau+\frac{\omega_0^2}{4}\right)\right] \times\int_{-\infty}^{\infty}\frac{dk_z}{(2\pi)^2}\exp\left[ik_zv_z\tau - |k_z|^2\left(D\tau+\frac{z_0^2}{4}\right)\right]. \quad (16)$$

In obtaining Eq. 16 we examine correlations only where $\mathbf{k}_\parallel = \mathbf{k}'_\parallel$. (See the Appendix for a detailed derivation.) Performing the integration in Eq. 16 yields:

$$\langle\tilde{i}(\mathbf{k}_\parallel,z;t)\tilde{i}^*(\mathbf{k}_\parallel,z;t+\tau)\rangle = \underbrace{N\frac{q^2I_0^2\omega_0^4\pi^2}{4}\langle\Theta(t)\Theta(t+\tau)\rangle\exp\left[i\mathbf{k}_\parallel\cdot\mathbf{v}_\parallel\tau - |\mathbf{k}_\parallel|^2\left(D\tau+\frac{\omega_0^2}{4}\right)\right]}_{\text{2 D model (Eq.13)}} \times\underbrace{\frac{z_0^2}{4\sqrt{\pi}\sqrt{4D\tau+z_0^2}}\exp\left[-\frac{v_z^2\tau^2}{4D\tau+z_0^2}\right]}_{\text{Additional 3D factor}}. \quad (17)$$

Thus, $r(\mathbf{k}_{||}, z;\tau, t)$ for a 3D sample (Eq. 17) is just the 2D result, cf. Eq. 13, multiplied by a factor, which accounts for the axial velocity of the particles and the geometry of the beam. Note that the 3D factor in Eq. 17 is constant for a given value of τ. Consequently, an image series sampled from a fixed lateral plane with particles undergoing 3D diffusion, or flow in the plane of imaging, can be analyzed in exactly the same way as a sample undergoing 2D diffusion or flow, and the correct diffusion coefficient and velocity will be recovered. In contrast to other fluorescence correlation techniques, the analysis of 3D diffusion with kICS does not require knowledge of the ratio of the axial beam waist to the lateral beam waist. The additional 3D factor must be taken into account to determine N or $\langle\Theta(t)\Theta(t+\tau)\rangle$ from a 3D sample.

Simulations

We generated simulations of LSM image time series to confirm that $\mathbf{v}$, D, and N for 2D and 3D samples could be determined as described above. We were able to accurately recover all three parameters for a variety of simulation conditions (data not shown).

Reversible photobleaching

It has recently been suggested that GFP variants, such as CFP and YFP, undergo a three-state reversible photobleaching (8):

$$\mathrm{XFP_{IB}} \overset{k_1}{\leftarrow} \mathrm{XFP_F} \underset{k_3}{\overset{k_2}{\rightleftharpoons}} \mathrm{XFP_{RB}}, \tag{18}$$

where $\mathrm{XFP_{IB}}$, $\mathrm{XFP_F}$, and $\mathrm{XFP_{RB}}$ are the irreversibly bleached, fluorescent, and reversibly bleached state of the fluorophore, respectively. The rate constants k_1, k_2, and k_3 correspond to the indicated transitions.

DATA ANALYSIS

One population

In the case of systems with one population undergoing diffusive flow, the correlation function corresponding to the diffusive transport, $\phi_d(|\mathbf{k}|^2, \tau)$, can be separated as follows:

$$\phi_d(|\mathbf{k}|^2,\tau) = \sqrt{(Re[r(\mathbf{k},\tau)])^2 + (Im[r(\mathbf{k},\tau)])^2} \tag{19}$$

$$= N\langle\Theta(t)\Theta(t+\tau)\rangle \frac{q^2 I_0^2 \omega_0^4 \pi^2}{4} \exp\left[-|\mathbf{k}|^2\left(\frac{\omega_0^2}{4} + D\tau\right)\right], \tag{20}$$

cf. Eq. 13, where $Re[r(\mathbf{k}, \tau)]$ and $Im[r(\mathbf{k}, \tau)]$ denote the real and the imaginary parts of $r(\mathbf{k}, \tau)$, respectively. The portion of the correlation function corresponding to the flow transport of the population, $\phi_f(\mathbf{k}, \tau)$, can then be separated by calculating:

$$\phi_f(\mathbf{k},\tau) = \frac{r(\mathbf{k},\tau)}{\phi_d(|\mathbf{k}|^2,\tau)} \tag{21}$$

$$= \exp[i\mathbf{k}\cdot\mathbf{v}\tau]. \tag{22}$$

Diffusion

To improve the S/N of the measurement, we calculate the diffusion coefficient by circularly averaging $\phi_d(|\mathbf{k}|^2, \tau)$, and then taking the natural logarithm of both sides of Eq. 20:

$$\ln[\phi_d(|\mathbf{k}|^2,\tau)] = \ln\left[N\langle\Theta(t)\Theta(t+\tau)\rangle q^2 \frac{I_0^2\omega_0^4\pi^2}{4}\right] - |\mathbf{k}|^2\left(\frac{\omega_0^2}{4} + D\tau\right). \tag{23}$$

Circular averaging is accomplished by averaging values of the correlation function with identical $(|\mathbf{k}|^2, \tau)$ values, where $|\mathbf{k}|^2 = k_x^2 + k_y^2$. Because the correlation functions are generated from the Fourier transforms of discretely sampled images, there are a finite number of (k_x, k_y) lattice points. For each time lag, τ, a linear fit of $\ln[\phi_d(|\mathbf{k}|^2, \tau)]$ as a function of $|\mathbf{k}|^2$ is performed. As $|\mathbf{k}|^2$ and τ increase, the particle-particle correlations become insignificant compared to noise. We have found the data is fit well by a first order spline with three knots, in which the first segment models the diffusive decay, and the second segment models the noise. This analysis is performed for each temporal lag of the correlation function, and the slope for the first segment, $-((\omega_0^2/4)+D\tau)$, is calculated for each lag (see Fig. 2).

Next, these slopes, $-((\omega_0^2/4)+D\tau)$, are plotted as a function of time lag, τ. The slope from the linear regression of this plot yields $-D$, while the intercept is $-(\omega_0^2/4)$, which can be used to determine the beam waist. Only the linear region of the plot is used, and the data are weighted using the errors returned from the linear regressions of Eq. 23 for each value of τ.

This analysis could also be used with data from a scanning FCS (SFCS) experiment. In this case, a 1D spatial Fourier transform can be performed along each scan cycle in the data series. The resulting transforms are correlated, in time, with each other. The analysis would then proceed exactly as presented above, where the wavenumbers are averaged over one line, instead of an image.

Flow

The velocity, $\mathbf{v}$, can be extracted by first taking the phase, θ, of the complex correlation function:

$$\theta(\mathbf{k},\tau) = \arctan\left[\frac{Im[\phi_f(\mathbf{k},\tau)]}{Re[\phi_f(\mathbf{k},\tau)]}\right] \tag{24}$$

$$= \mathbf{k}\cdot\mathbf{v}\tau. \tag{25}$$

Because inverse tangent functions have limited ranges (an interval of $[-\pi, \pi]$, in the case of atan2), $\theta(\mathbf{k}, t)$ may have a saw-tooth appearance. This artifact can be corrected by adding multiples of $\pm 2\pi$ to adjacent values in $\theta(\mathbf{k}, t)$, which differ by more than a jump tolerance of π.

With experimental data, only the central (i.e., low $|\mathbf{k}|^2$) portion of the correlation function contains useful data, because the entire function is damped by the exponential factor resulting from the convolution with the laser beam. After calculating and viewing $\phi_f(\mathbf{k}, t)$, it is clear where the noise predominates over the signal, and the data can be cropped

accordingly (cf. Fig. 5). The velocity can be determined from $\theta(\mathbf{k}, t)$ by calculating the gradient numerically, then averaging over all $\mathbf{k}$, dividing by τ, and finally averaging over all τ:

$$\mathbf{v} = \left\langle \frac{\langle \nabla\theta \rangle_{\mathbf{k}}}{\tau} \right\rangle_{\tau}, \tag{26}$$

where we use the gradient definition $\frac{\partial f}{\partial x} = \frac{f(x+\Delta)-f(x)}{\Delta}$. In practice, a numerical gradient returns the gradient in both the k_x and k_y directions, giving the components v_x and v_y, respectively. Alternatively, one could perform a linear least-squares fit to each component of the gradient of $\theta(\mathbf{k}, t)$ at different values of τ, recovering $v_x\tau$ and $v_y\tau$. The velocity components themselves can then be found by a linear regression as a function of τ.

Number densities

The reciprocal of the total average number of particles in an image series can be calculated by dividing Eq. 13 by the average total image intensity squared, in the limit of $|\mathbf{k}|^2 \to 0$,

$$\frac{r(0;t,\tau)}{(\Sigma_{p=1}^{P}(\Sigma_{x=1}^{X}\Sigma_{y=1}^{Y} i(x,y,p))/P)^2} = \frac{N\langle\Theta(t)\Theta(t+\tau)\rangle q^2 \frac{I_0^2\omega_0^4\pi^2}{4}}{N^2q^2I_0^2\langle\Theta(t)\rangle\langle\Theta(t+\tau)\rangle\left(\int_{-\infty}^{\infty} d\mathbf{r}\exp\left[-2\left(\frac{x^2+y^2}{\omega_0^2}\right)\right]\right)^2} \tag{27}$$

$$= \frac{\langle\Theta(t)\Theta(t+\tau)\rangle}{N\langle\Theta(t)\rangle\langle\Theta(t+\tau)\rangle} \tag{28}$$

$$= \frac{1}{N}, \tag{29}$$

where X and Y are the dimensions, in pixels, of the images and P is the number of images. The last equality holds when one assumes the particles are always emitting. If the fluorescence characteristics of the sample are known (i.e., $\langle\Theta(t)\rangle$ and $\langle\Theta(t)\Theta(t+\tau)\rangle$), these can be substituted in Eq. 28 to calculate an accurate number density even in the presence of complex bleaching or blinking (25). The $|\mathbf{k}|^2 = 0$ value is not used because it contains the DC component of the Fourier transforms. Instead, the intercept is determined by fitting. If the log transformation (Eq. 23) is used to extract the number density, care must be taken to ensure no bias in the intercept is introduced when retransforming (see Miller (26) for a discussion and correction of this effect). If the untransformed data are fit with a partitioned least-squares fit, no such bias is introduced (data not shown). Furthermore, the total image intensity used in the normalization is background subtracted.

Multiple populations

For a sample with M different populations, $r(\mathbf{k}, \tau)$ has the following form:

$$r(\mathbf{k},\tau) = \frac{I_0^2\omega_0^4\pi^2}{4}\exp\left[\frac{-|\mathbf{k}|^2\omega_0^2}{4}\right]\sum_{m=1}^{M} N_m q_m^2\langle\Theta_m(t)\Theta_m(t+\tau)\rangle \times \exp[(i\mathbf{k}\cdot\mathbf{v}_m - |\mathbf{k}|^2 D_m)\tau], \tag{30}$$

where D_m is the diffusion coefficient, $\mathbf{v}_m$ is the velocity, and $\Theta_m(t)$ and q_m are the fluorescing factors $\Theta(t)$ and q of the m^{th} population of N_m particles. Equation 30 assumes the particles within a given population have the same fluorescence characteristics.

In cells, two populations are often present: one flowing population, and one diffusing population. In this case, $r(\mathbf{k}, \tau)$ has the following form:

$$r(\mathbf{k},\tau) = \frac{I_0^2q^2\omega_0^4\pi^2}{4}\langle\Theta(t)\Theta(t+\tau)\rangle\exp\left[\frac{-|\mathbf{k}|^2\omega_0^2}{4}\right] \times (N_f\exp[i\mathbf{k}\cdot\mathbf{v}\tau] + N_d\exp[-|\mathbf{k}|^2 D\tau]), \tag{31}$$

where N_f is the number of flowing particles, and N_d is the number of diffusing particles, and both populations are assumed to have the same fluorescence properties. To extract the velocity of the flowing component, each time lag of the imaginary part of the correlation function can be divided by the real part of the $\tau = 0$ lag:

$$r_f(\mathbf{k},\tau) = \frac{Im[r(\mathbf{k},\tau)]}{Re[r(\mathbf{k},0)]} \tag{32}$$

$$= \frac{N_f}{N_f+N_d}\sin[\mathbf{k}\cdot\mathbf{v}\tau]. \tag{33}$$

A nonlinear fit of r_f ($\mathbf{k}$, τ) to Eq. 33 for each value of τ allows v_x and v_y to be determined.

MATERIALS AND METHODS

Fluorescent microsphere solution preparation

Aqueous solutions of sucrose (Sigma-Aldrich, Oakville, Ontario, Canada) were prepared in milliQ distilled water. A stock solution of microspheres (Molecular Probes, Burlington, Ontario, Canada) was sonicated for 15 min before use. Sample solutions were prepared by adding 198 μL of a sucrose solution to 2 μL microsphere stock solution, giving sucrose concentrations ranging from 668 to 796 g/L, and viscosities ranging from 18.6 to 60.2 mPa s. Viscosities were determined using Dean (27). The diluted microsphere solution was sonicated for an additional 15 min before being pipetted into the cavity of a glass-bottomed petri dish (No. 1.5; MatTek, Ashland, MA) for imaging. The cavity was sealed with a coverslip. The fluorescent microspheres were carboxylate coated with a radius of (0.105 $\pm$ 0.005) μm, an excitation maximum of 505 nm, and an emission maximum of 515 nm. The uncertainty associated with the microsphere radius was supplied by the manufacturer.

The theoretical diffusion coefficients for the fluorescent microspheres were determined using the Stokes-Einstein equation:

$$D = \frac{k_B T}{6\pi\eta R}, \tag{34}$$

where k_B is Boltzmann's constant, T is absolute temperature, η is the solvent viscosity, and R is the microsphere radius.

Cell culture

CHO-K1 cells were transfected to express α5-integrin/eGFP as previously described (28) (provided by A. R. Horwitz, University of Virginia). Cells were cultured in Dulbecco's modified Eagle's medium, supplemented with

10% fetal bovine serum, 4 mM L-glutamine, 100 units/ml penicillin, 0.1 mg/ml streptomycin, 0.1 mM nonessential amino acids, and 0.5 mg/ml G418 to maintain transfection (Gibco, Carlsbad, CA). Cells were incubated in 5.0% CO_2 atmosphere at 37°C. For imaging, cells were plated on 10 μg/mL fibronectin coated glass-bottomed petri dishes (No. 1.5; MatTek, Ashland, MA).

Confocal microscopy

Samples were imaged with an Olympus FV300 IX71 confocal laser scanning microscope (Olympus, Melville, NY), using the 488-nm laser line of an Ar^+ laser for excitation. Fluorescence was collected by a 60× PlanApo oil immersion objective (NA 1.4) using a 488-nm bandpass dichroic in combination with a BA510IF long-pass filter (Chroma, Rockingham, VT). Image series were collected with a zoom that gave a pixel resolution 0.115 μm, with 0.451 s between consecutive scans. The PMT was adjusted such that no pixels were saturated, and no thresholding was applied.

Total internal reflection microscopy

Cells were imaged at room temperature on an Olympus IX71 microscope with a TIRF illuminator. Excitation was provided by the 488-nm line of an Ar^+ laser, and an evanescent wave was formed by changing the angle at which the beam entered a 60× Plan Apochromat oil immersion lens (1.45 NA, Olympus, Melville, NY). Fluorescence was collected by the objective, and imaged onto a cooled back-illuminated Cascade 512B CCD camera (Roper Scientific, Tucson, AZ). Frame integration times were 50 ms with an on-chip gain of 3000, with 1 s between subsequent images. Image series were 512 × 512 pixels^2 × 100 images, with a pixel resolution of 0.163 μm.

Simulations and data analysis

Simulations, and the calculation and analysis of reciprocal-space time correlation functions, were performed as described in the Theory and Results sections on a personal computer (2.4 GHz, 1GB RAM), using custom MATLAB R14 (The MathWorks, Natick, MA) routines.

The simulation program has been described in detail previously (25). Briefly, it simulates the point source emitters undergoing flow, 2D, or 3D diffusion, which are imaged on a system with a 2D or 3D Gaussian PSF (convolution function). The program allows one to control the size of the convolving function, the amount of noise, and the bleaching characteristics of the emitters, among other features.

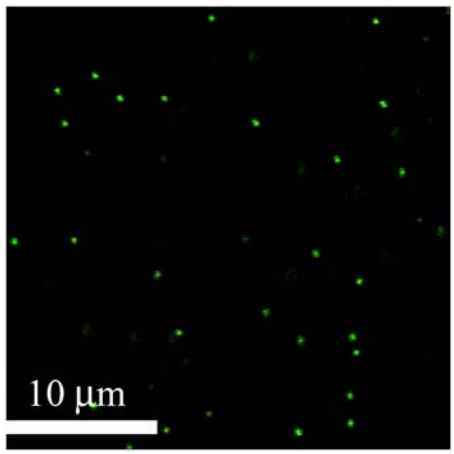

FIGURE 1 A 256 × 256 pixel^2 CLSM image of 0.105 μm radius fluorescent microspheres (505 nm excitation / 515 nm emission) in aqueous sucrose solution. The 488-nm line of a He-Ne laser was used for excitation, and fluorescence was collected using a 510-nm long-pass filter. The pixel size was 0.115 μm.

RESULTS

Microsphere measurements

Fig. 1 shows an image of 0.105 μm diameter fluorescent green microspheres in sucrose solution obtained on a CLSM. The $r(\mathbf{k}, \tau)$ was calculated from this image series using Eq. 10. The first temporal lag, $r(\mathbf{k}, 0.451\text{s})$ is shown in Fig. 2 *A*, as an example. When the natural logarithm of $r(\mathbf{k}, \tau)$ for a given τ is circularly averaged over $|\mathbf{k}^2|$, a linear relationship is evident (Fig. 2 *B*), as expected from Eq. 23. In this case, the linear regression gave a slope of -0.0312 μm^2. An analogous linear regression is performed for each temporal lag in $r(\mathbf{k}, \tau)$.

In Fig. 2 *B*, the data were fit to a first-order spline with three knots, where the first segment modeled the signal and the second segment modeled the noise. The crossover point between these two segments (i.e., the second knot of the

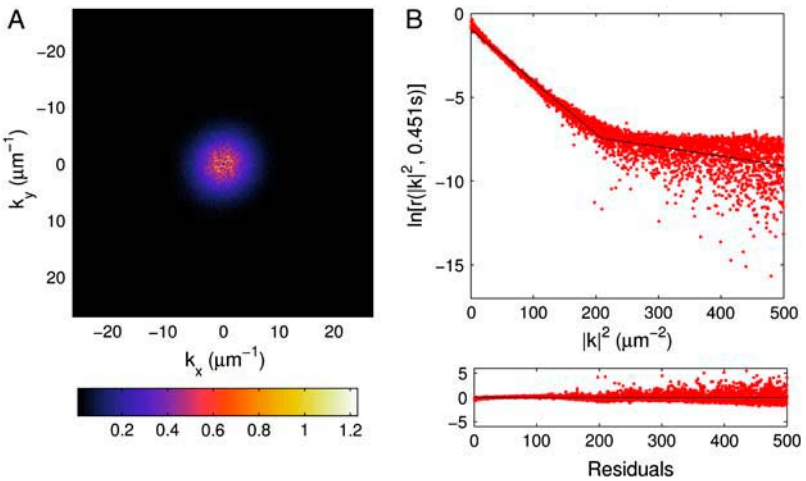

FIGURE 2 The reciprocal space correlation function $r(k_x, k_y, \tau)$ for lag $\tau = 0.451$ s of a diffusing microsphere sample both (*A*) before and (*B*) after circularly averaging and taking the natural logarithm. The data was fit to Eq. 23, and the slope of the first segment is $-(\omega_0^2/4+D\tau)$. In this case, the first segment of the circularly averaged correlation function has a line of best fit of $r(|\mathbf{k}|^2, 0.451\text{ s}) = -0.0312\ \mu\text{m}^2|\mathbf{k}|^2 - 0.930$. The $(k_x, k_y) = (0, 0)$ point, which corresponds to the DC component of the Fourier transforms, has been omitted in these figures, and is not used for fitting.

spline) provides a useful measure of the S/N of the measurement. As the number of pixels in the region of analysis decreases, the length of the first linear region of the correlation function will decrease. As well, a decrease in brightness of the particles, an increase in the noise level, or a larger PSF of the imaging system will shift the crossover point to lower $|\mathbf{k}|^2$ values (simulation data not shown). kICS analysis can only be performed if the first segment can be fit to a straight line. Under our imaging conditions, the minimum size was $\sim 32 \times 32$ pixels^2.

The slopes of each correlation function at different τ-values were then plotted as a function of τ (Fig. 3). The statistical error from the linear regressions of $r(\mathbf{k}, \tau)$ at a given τ provide the error bars, which are used as weights when fitting. The so-called slope of the slopes immediately yields D, which was 0.0316 ± 0.0002 μm^2/s. The intercept from the regression was -0.023 μm^2, which corresponds to an ω_0 value of 0.304 μm.

To rigorously investigate the accuracy of this technique, we prepared microsphere samples in five different concentrations of sucrose in distilled water. For each concentration, 10 image series of 256×256 pixels^2 by 250 images were collected and analyzed. The results are presented in Fig. 4, by plotting the experimentally determined D as a function of D predicted using the Stokes-Einstein relationship (Eq. 34). The linear regression of the data in Fig. 4 yielded a line with slope 1.07. The average of all of the intercepts, $\langle -\frac{\omega_0^2}{4} \rangle$, from the correlation functions of these image series was -0.05 ± 0.01 μm^2, which gives $\langle \omega_0 \rangle = 0.43 \pm 0.05$ μm. This value is comparable to that measured independently. The relative standard deviation for the determination of ω_0 was 12%, and the relative standard deviation for all of the D-values was 12%. Using the Stokes-Einstein relationship (Eq. 34), values of D recovered with kICS gave a $\langle R \rangle$ of 0.102 ± 0.004 μm, agreeing with the manufacturer's stated radius of 0.105 ± 0.005 μm.

To show that the velocity of a flowing population can be measured, we collected an image time series of fluorescent particles undergoing flow. The image series size was 256×256 pixels^2 by 100 images; it had a pixel size of 0.115 μm and a sampling rate of 2.22 Hz. Using Eq. 10, $r(\mathbf{k}, \tau)$ was calculated and the flowing component of the function was separated from the diffusive component and exponential beam modulation (cf. Eq. 21). The resulting $\varphi_f(\mathbf{k}, \tau)$ is shown for one time lag in Fig. 5. As expected, the real component (Fig. 5 *A*) was a cosine wave, while the imaginary component (Fig. 5 *B*) was a sine wave. To extract the phase of the complex exponential, the arc-tangent of the quotient of the two components was calculated (Eq. 24). This phase is given by $\mathbf{k}\cdot\mathbf{v}\tau$, and forms a plane that increases in

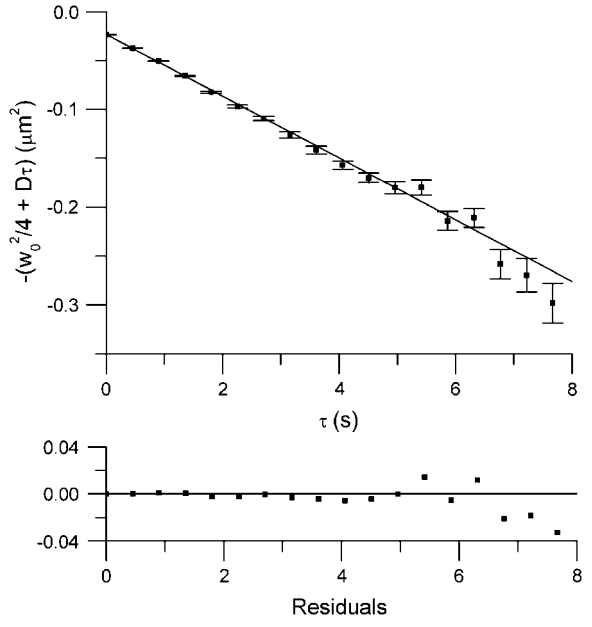

FIGURE 3 Slopes recovered from Eq. 23 at each time lag τ, $-(\omega_0^2/4 + D\tau)$, plotted as a function of τ for a sample of diffusing fluorescent microspheres. The slope of this plot is $-D$, whereas the intercept is $-\omega_0^2/4$. In this case, D was 0.0316 ± 0.0002 μm^2/s, and the value of ω_0 extracted from the intercept was 0.304 ± 0.001 μm. The error bars are the error of the corresponding linear regressions (see Fig. 2 *B*), and the regression in this plot was weighted using these errors.

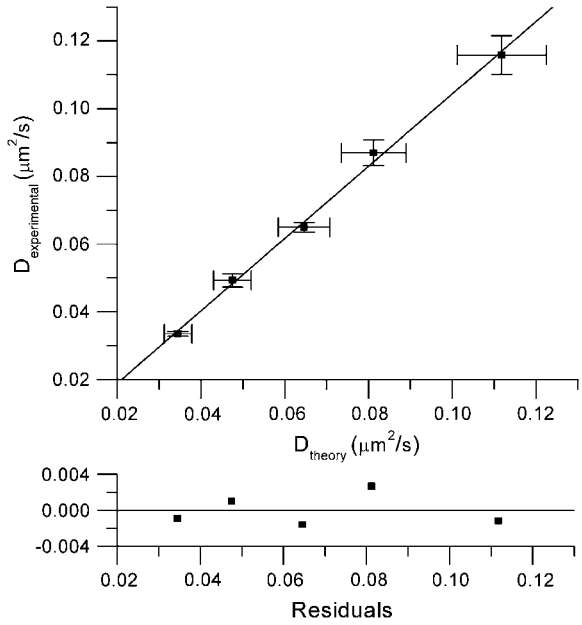

FIGURE 4 A plot of D of microspheres in aqueous sucrose solution, measured using kICS as a function of the theoretically predicted D from the Stokes-Einstein relationship (Eq. 34). D was varied in each sample by changing the concentration of sucrose, while keeping the microsphere size and temperature constant. The line of best fit is $D_{\text{experimental}} = 1.07\ D_{\text{Stokes-Einstein}} - 0.0024$ μm^2/s, with an R^2 value of 0.997. Each point is an average of 10 results from analyses of image series of 256×256 pixels^2 by 250 images. The pixel size in all image series was 0.115 μm, and the temporal sampling rate was 2.22 Hz. Error bars in the experimentally determined diffusion coefficient are mean $\pm$ SE, and error bars in theoretical diffusion coefficient are propagated from the uncertainty in the radius of the microspheres.

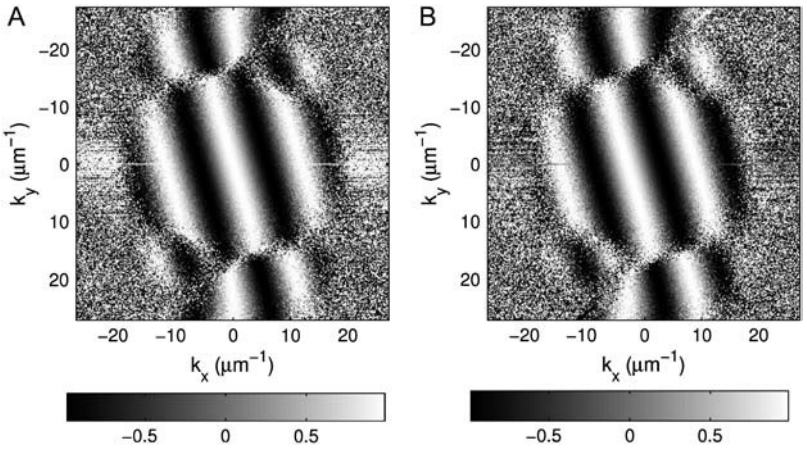

FIGURE 5 The (*A*) real and (*B*) imaginary components of $r(\mathbf{k}, 0.451\ \text{s})$ for an image series of fluorescent microspheres undergoing flow as a function of k_x and k_y. The exponential modulation due to the laser beam convolution has been removed (see Eq. 21), which results in noise at higher values of k_x and k_y. The image series size was 256×256 pixels^2 with 100 images, a pixel size of 0.115 μm, and a sampling rate of 2.22 Hz.

the direction of the movement (Fig. 6, *A–D*). A one-parameter linear least-squares fit of the numerical gradient over this surface for a particular value of τ gives the product of τ with both directional components of the velocity: $v_x\tau$ and $v_y\tau$. This procedure is repeated for each value of τ. A linear regression of $v_x\tau$ and $v_y\tau$ as a function of time lag gives v_x and v_y (Fig. 6 *E*). In this example, the linear regression gave slopes of $v_x = -1.133 \pm 0.003$ μm/s, $v_y = 0.288 \pm 0.003$, and $|\mathbf{v}| = 1.169 \pm 0.003$ μm/s. SPT analysis was carried out on the same image series (SPT algorithm from Crocker and Grier (29)), yielding $|\mathbf{v}| = 1.1 \pm 0.1$ μm/s (66 trajectories).

The preceding analysis can be performed when there is only one population present and it is flowing, or if there is an immobile fraction in addition to the flowing population. In the latter case, the immobile component can be removed by Fourier filtering (30). However, if one population of particles is diffusing and another flowing, a different approach must be taken. First, the imaginary part of the correlation function is separated from the exponential beam modulation (Eq. 33). Next, for each value of τ, a partitioned one-parameter nonlinear fit was performed to the data, yielding $v_x\tau$, $v_y\tau$, and N_f/N_f+N_d. Linear regressions of $v_x\tau$ and $v_y\tau$ as a function of τ yield v_x and v_y, respectively (Fig. 7).

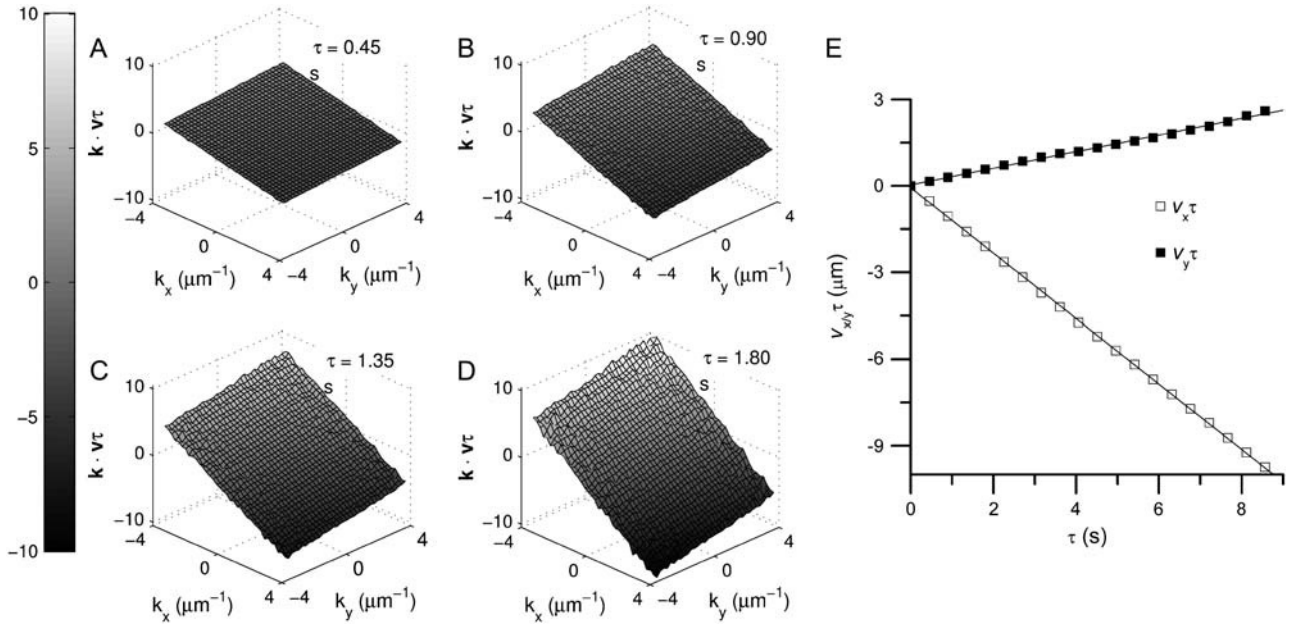

FIGURE 6 The phase of the complex exponential portion of $r(\mathbf{k}, \tau)$, $\mathbf{k}\cdot\mathbf{v}\tau$, of an image series of flowing fluorescent microspheres as a function of k_x and k_y for temporal lags (*A*) 0.451 s, (*B*) 0.902 s, (*C*) 1.353 s, and (*D*) 1.804 s. The phase was extracted using the inverse tangent of the quotient of the imaginary and real components of the correlation function (cf. Eq. 24). It forms a plane, increasing in the direction of the flow, with a steepness proportional to τ. (*E*) Plots of the $v\tau$ values recovered from one-parameter linear least-squares fitting to the numerical gradients of $\mathbf{k}\cdot\mathbf{v}\tau$, $v\tau$, for both x and y directions as a function of temporal lag, for the first 20 lags. A linear regression yields the velocity components, $v_x = -1.133 \pm 0.003$ μm/s, and $v_y = 0.288 \pm 0.003$ μm/s.

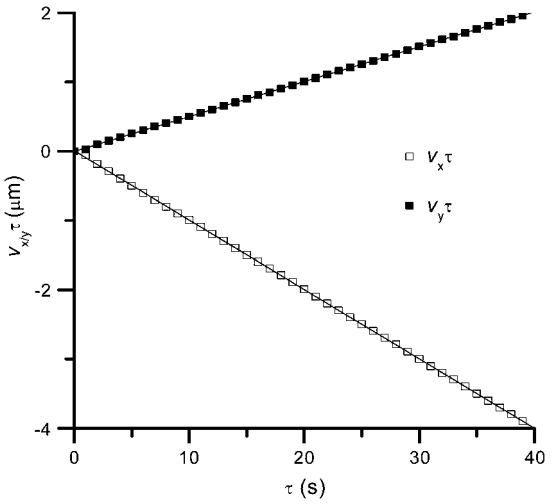

FIGURE 7 Fitted parameters of $v_x\tau$ and $v_y\tau$ as a function of τ from a nonlinear fit of each temporal lag of $r(\mathbf{k}, \tau)$ to Eq. 33 for a simulation of flowing and diffusing particle populations. A linear regression of these values as a function of τ (shown) yields $v_x = -0.1001$ μm/s and $v_y = 0.0504$ μm/s, when the set parameters were -0.1000 μm/s and 0.0500 μm/s, respectively. The simulation consisted of 256 $\times$ 256 pixels^2 with 100 images at an imaging rate of 1 Hz, a PSF with an e^{-2} radius of 0.4 μm, a flowing population of five particles μm^{-2}, and a diffusing population of five particles μm^{-2} with $D = 0.01$ μm^2/s.

Simulations of reversible photobleaching

To investigate the ability of kICS to recover accurate dynamics in the presence of photobleaching, we created simulations that modeled the reversible bleaching of eCFP, eYFP, and citrine using rate constants reported by Sinnecker et al. (8). An example of the mean intensity of these bleaching processes is included in Fig. 8 *A*, and the diffusion coefficients calculated using both TICS (without using photobleaching correction from Kolin et al. (25)) and kICS are included in Fig. 8 *B*.

Simulations of the determination of number densities from heterogeneous samples

The spatial distribution of fluorescently labeled membrane proteins in a living cell is frequently heterogeneous. To determine the sensitivity of kICS to the spatial arrangement of particles, we generated sets of image series of particles with different spatial distributions (Fig. 9, *A–F*), and then calculated the number densities using kICS. We also measured the densities using spatial ICS, an established technique for extracting number densities from labeled membrane proteins (16). Both techniques work well when the particles are distributed uniformly, however, they both returned biased results when the particles are not uniformly distributed (Fig. 9 *G*). In these cases, however, kICS returned significantly more accurate results than spatial ICS.

Live cell measurements

To show the applicability of kICS to live cell measurements and area detection-based imaging, we collected a TIRFM image series of the basal membrane of a CHO cell expressing α5-integrin/eGFP (Fig. 10 *A*). The mean of an off-cell region was subtracted from the image series to correct for scattered light and CCD bias. A large fraction of α5-integrin is known to be immobile on the timescale of 1–2 min (28). Consequently, we removed the immobile fraction before analysis as previously described (30). The eGFP exhibited bleaching such that the mean intensity of the region analyzed decreased by ~60% (Fig. 10 *B*).

The reciprocal-space time correlation function was calculated as with the microsphere sample, and a D of 0.0096 $\pm$ 0.0002 μm^2/s was measured (Fig. 11). No flow was detected in this subregion of the cell using kICS.

To show that photobleaching parameters could be determined independently of dynamics, a $\langle\Theta(t)\Theta(t+\tau)\rangle$ correlation function was calculated for each of nine cells, by finding the intercept as $|k|^2 \to 0$ of Eq. 23 for each pair of images in each image series. These functions were normalized assuming all the particles were fluorescent at $t = 0$, and averaged over nine regions obtained from different cells (Fig. 12 *A*). If the photobleaching is a first-order process, then

$$\ln[\langle\Theta(t)\Theta(t+\tau)\rangle] = -2kt - k\tau, \tag{35}$$

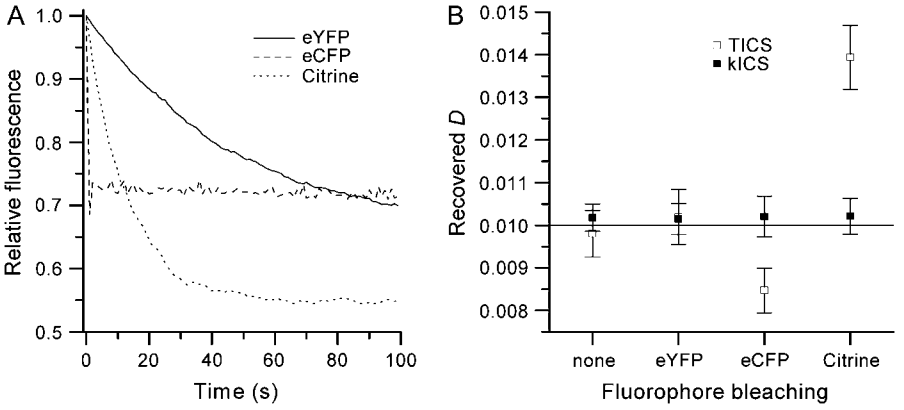

FIGURE 8 (*A*) Plots of mean intensities as a function of time for image series simulations of eCFP, eYFP, and citrine reversible photobleaching kinetics. (*B*) Mean diffusion coefficients recovered from both TICS and kICS analyses of 100 simulations of each type of fluorophore. The set D was 0.01 μm^2/s, and each simulation was 256 $\times$ 256 pixels^2 $\times$ 100 images, with $\omega_0 = 0.4$ μm and 10 particles μm^{-2}. Error bars are mean $\pm$ SD.

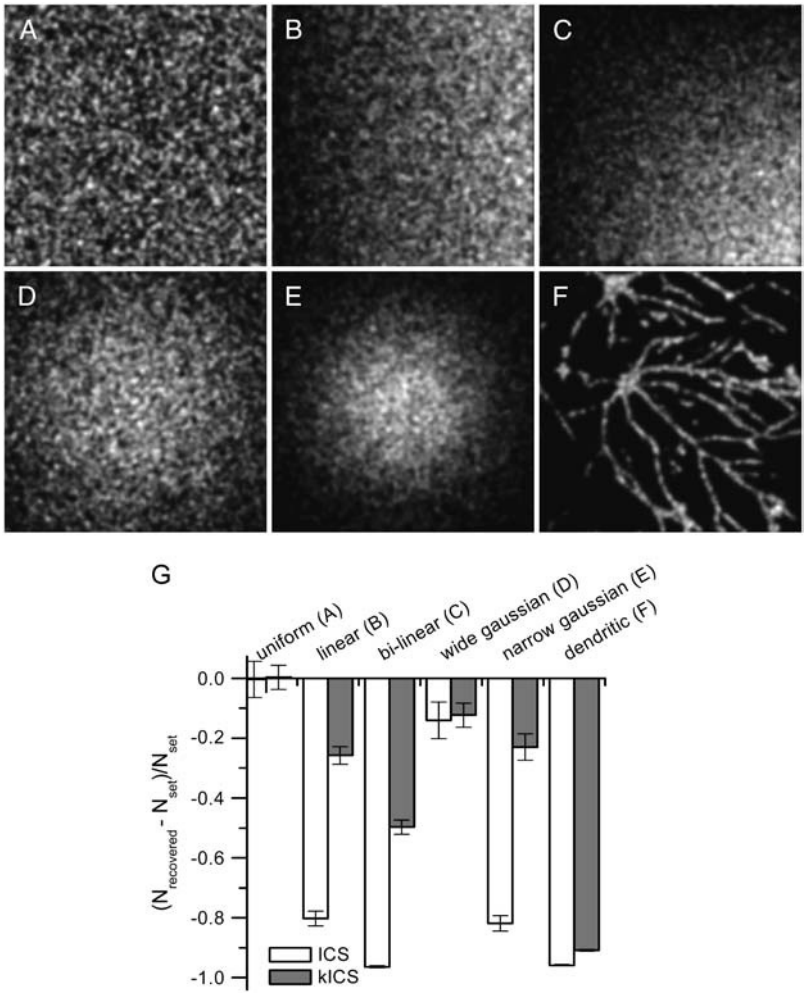

FIGURE 9 Simulated images of particles distributed with different spatial arrangements: (*A*) uniformly, (*B*) linearly in one direction, (*C*) linearly in both directions, (*D*) a slowly decaying Gaussian, (*E*) a quickly decaying Gaussian, and (*F*) a dendritic arrangement similar to a neuronal sample. Each image is 256×256 pixels^2, with $\omega_0 = 0.4$ μm and a pixel size of 0.1 μm. (*G*) Number densities recovered from spatial ICS and kICS analyses of uniformly and nonuniformly distributed particles, as pictured in panels *A–F*. Because the number of particles varied slightly in each simulated image, the accuracy of the results is reported as a fractional error. Each bar is the mean result of the analysis of 100 images, and error bars are mean ± SD.

where k is the rate constant. To verify this relationship, select values of ln $[\langle\Theta(t)\Theta(t+\tau)\rangle]$ were plotted by holding either t (Fig. 12 *B*) or τ (Fig. 12 *C*) at a fixed value. If the bleaching was indeed a first-order process, Eq. 35 suggests that the regression lines in Fig. 12 *B* should have slopes half as large as, and intercept spacings between adjacent lines twice as large as those in Fig. 12 *C*. To rigorously investigate this, we performed linear regressions of ln $[\langle\Theta(t)\Theta(t+\tau)\rangle]$ for each value of t and τ, analogous to those shown in Fig. 12, *B* and *C*. The mean value of the slopes of ln $[\langle\Theta(t)\Theta(t+\tau)\rangle]$ at fixed t values was -0.008 ± 0.001 s^{-1}, and mean spacing between adjacent intercepts was 0.02 ± 0.01. When τ was fixed, these values were -0.015 ± 0.001 s^{-1}, and 0.011 ± 0.004, respectively. Using Eq. 35 and these four values, a

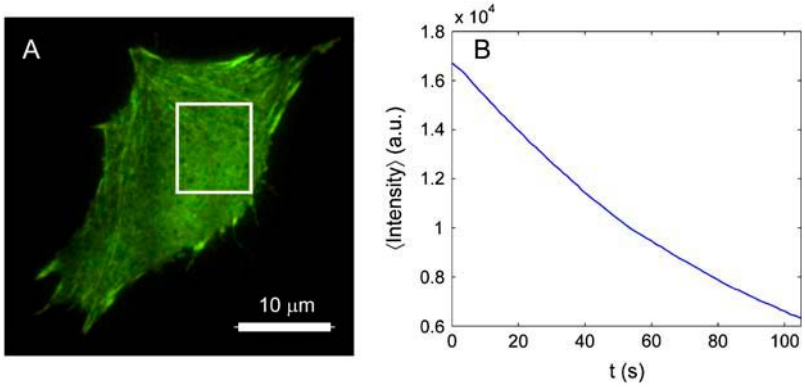

FIGURE 10 (*A*) TIRFM image of α5-integrin/eGFP expressed in a CHO cell plated on 10 μg/mL fibronectin. The 90×65 pixel^2 region used for kICS analysis is outlined. The image series consisted of 100 images, with 50 ms integration time per image and 1 s between successive images. (*B*) The average image intensity of the outlined region in panel *A* as a function of time.

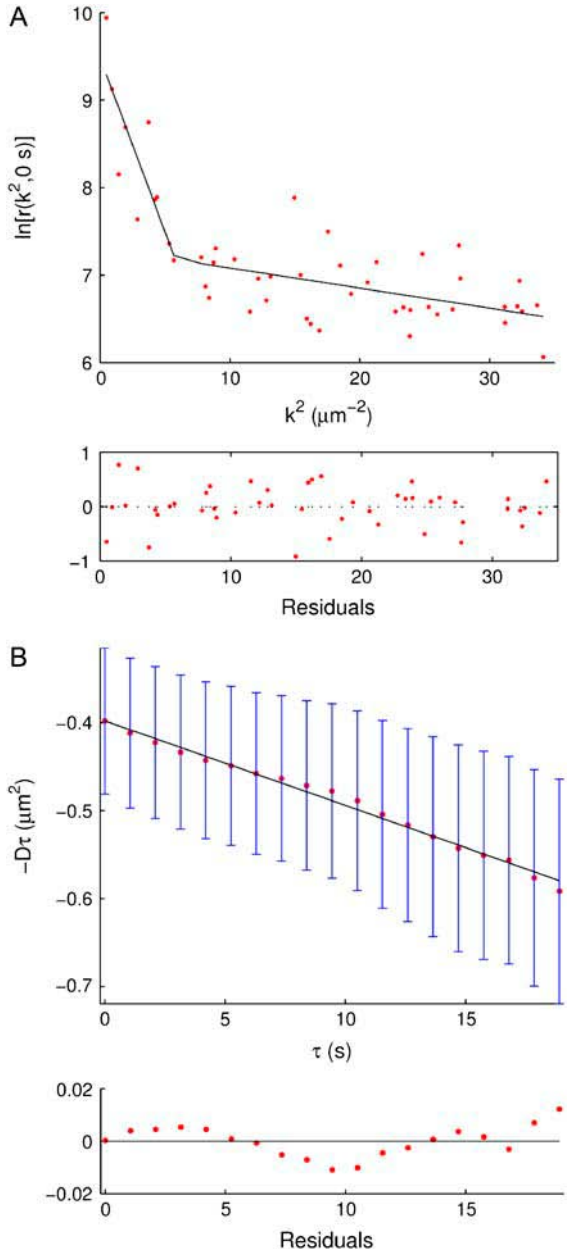

FIGURE 11 (*A*) Natural logarithm of the circularly averaged k-space correlation function at equal times ($\tau = 0$ s) for the region of the cell outlined in Fig. 10. Assuming a diffusive model, the first linear segment is given by $-(\omega_0^2/4+D\tau)$. By fitting each temporal lag of the correlation function as here, one can extract D. (*B*) Determination of D from the image series of the cell in Fig. 10. D was given by the slope, and was 0.0096 ± 0.0002 μm^2/s.

weighted average value of k was calculated to be 0.008 ± 0.002 s^{-1}.

The averaging over nine cells, as performed above, is an unbiased estimator of $\langle\Theta(t)\Theta(t+\tau)\rangle$ only if there are a large enough number of independent fluctuation domains (i.e., PSFs) in the image areas, and if the assumed model, e.g., Eq. 13, is valid (e.g., the particles must be statistically independent). To show that this method of averaging was acceptable in our case, we repeated the calculation of $\langle\Theta(t)\Theta(t+\tau)\rangle$ by first Fourier transforming the images, and then averaging $\tilde{i}(\mathbf{k},t)\tilde{i}^*(\mathbf{k},t+\tau)$ over the nine data sets before fitting. This method is slightly more computationally intensive, but is more rigorous than the post-fitting averaging described previously, and in principle can deal with correlated dynamics. Nonetheless, it is much simpler to deal with different size images in the first method (i.e., when the grid of wavevectors varies from image to image). The second method of analysis yielded a $\langle\Theta(t)\Theta(t+\tau)\rangle$ nearly identical to that presented in Fig. 12. The rate constant calculated from this correlation function was 0.008 ± 0.001 s^{-1}, which agrees with the previous calculation and has a slightly smaller standard deviation.

The rate constant was also determined by fitting the average intensity to a monoexponential decay for each of the nine image series. The mean k obtained using this method was 0.007 ± 0.001 s^{-1}, in agreement with the value obtained using kICS.

DISCUSSION

Accurate measurements of transport coefficients in the presence of fluorophore bleaching and blinking

As can be seen in Eqs. 23 and 26, the transport coefficient D and $\mathbf{v}$ can be extracted independently of $\Theta(t)$, which models the blinking and photobleaching characteristics of the fluorophore. The simulations presented confirm this for reversible photobleaching (Fig. 8 *B*). Previously, accurate transport coefficients could only be recovered via TICS if the bleaching process could be well-characterized by the average intensity of the image series as a function of time (25). Although this previous method also allows for the accurate recovery of number densities, it requires that the average intensity of the image series be satisfactorily fit by a functional form, and it assumes that the bleaching is irreversible on the image series acquisition timescale. Recently, Sinnecker et al. (8) showed that eCFP and eYFP exhibit reversible photobleaching on timescales applicable to FRAP and TICS analyses. FRAP experiments can return erroneous mobile fractions and diffusion coefficients as a direct result of this reversible bleaching (8). Furthermore, the photobleaching correction previously proposed for TICS analyses cannot be applied to reversible bleaching, so the results will be biased in a manner similar to irreversible photobleaching (25).

No assumptions are made with kICS regarding the relative values of $\Theta(t)$ and $\Theta(t+\tau)$ for a fluorophore. Indeed, we have shown this technique can still recover accurate transport parameters in the presence of reversible photobleaching. Furthermore, this technique also works for intermittent fluorescence (''blinking''), which is a hallmark of quantum dot nanoparticles. This can result in a nonstationary and erratic behavior for $\langle\Theta_i(t)\Theta_i(t+\tau)\rangle$ (A. Bashir, D. Kolin,

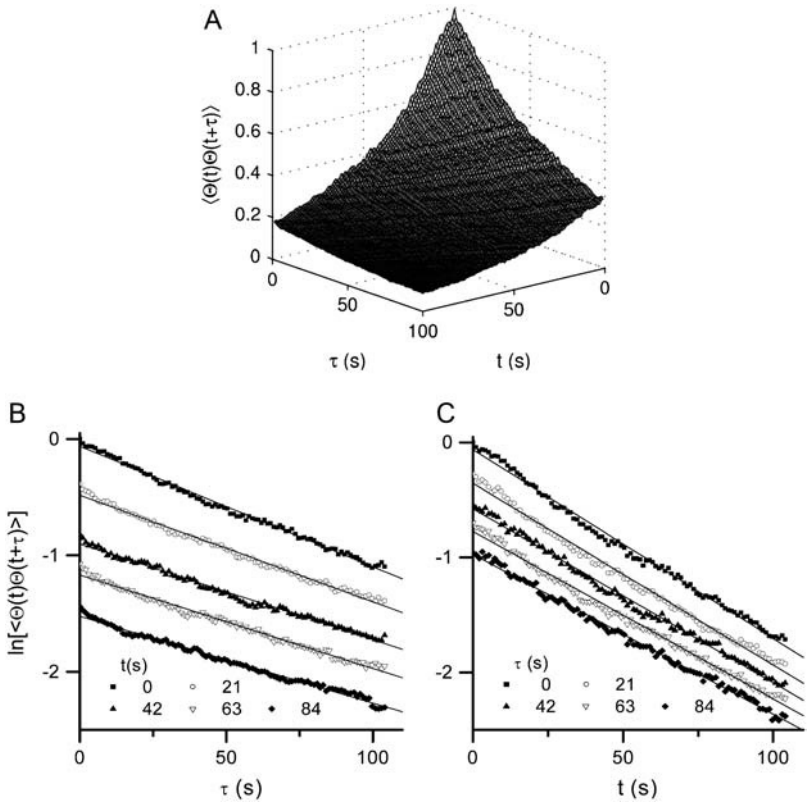

FIGURE 12 (*A*) The $\langle\Theta(t)\Theta(t+\tau)\rangle$ correlation function, as a function of t and τ, for an ensemble of nine cells. The values were obtained from the intercept of Eq. 23 for pairs of images at time t and $t+\tau$. The function was normalized assuming all particles were fluorescent at $t=0$, and was averaged over all nine data sets, but not over either t or τ. The natural logarithm of $\langle\Theta(t)\Theta(t+\tau)\rangle$ plotted for five fixed values of t (*B*) and τ (*C*). The slope and intercept of each linear regression were used to calculate the photobleaching rate constant (see text).

B. Hebert, P. Wiseman, unpublished data). Because QDs blink on all timescales, attempts to fit temporal intensity fluctuation decays to diffusive models can be frustrated by the fluctuations introduced by the blinking (13). However, for kICS, this factor is not a concern when calculating D or $\mathbf{v}$, because they are extracted independently of $\langle\Theta_i(t)\Theta_i(t+\tau)\rangle$. Any bleaching or blinking would only change the intercept of Eq. 23, and not the slope, which is used for determining D. Similarly, if Eq. 20 is used to separate the diffusive and flowing components of the correlation function, then the optical characteristics are independent of the flow component of the correlation function. It should be emphasized that this analysis does not require a case-by-case correction, which depends on the type or rate of fluorescence intermittency. The data is analyzed in exactly the same way regardless of any photobleaching or blinking present, and an accurate transport coefficient is returned. We believe this will be especially advantageous to life sciences researchers who wish to accurately measure dynamics of fluorescently tagged proteins without quantifying and attempting to correct for their bleaching or blinking properties. Furthermore, it allows fluorophore selection to be based on criteria such as brightness, labeling efficiency, and spectral characteristics, without focusing on the photostability of potential fluorophores. There are a number of antifade reagents available for fixed samples, which reduce the severity of photobleaching (31). However, these are often not suitable for live cell imaging.

If bleaching or blinking is nonnegligible, one cannot calculate accurate number densities from the time correlation function without knowing the value of $\langle\Theta_i(t)\Theta_i(t+\tau)\rangle$ and $\langle\Theta_i(t)\rangle$, quantities that can only be calculated directly from the image series if the bleaching is irreversible. In this case, an accurate particle count can be recovered by dividing the total intensity of the first image squared by its power spectrum in the limit $|\mathbf{k}|\rightarrow 0$, assuming that all fluorophores are in their ''on'' state at $t=0$. We predict that kICS will be a useful tool to probe the bleaching and blinking of fluorophores, because the value of the intercept from Eq. 23 is directly related to the photophysical dynamics of the fluorophore ($\langle\langle\Theta_i(t)\Theta_i(t+\tau)\rangle\rangle$). In this work, we showed how the photobleaching rate of GFP in a live cell could be determined independently of the fluorophore dynamics. We were able to measure this quantity, even though the photobleaching and translational dynamics occurred on similar timescales.

Independence of D, $\mathbf{v}$, and N from ω_0

Calculation of dynamics and number densities in the Fourier domain is both a more robust and precise technique than its traditional spatial domain counterpart. The transport coefficients and number density can be calculated without any knowledge of the beam radius. The determination of these parameters via kICS is in contract to ICS, TICS, FCS, or spot FRAP in which there is a dependence of D, $\mathbf{v}$, and $\langle N\rangle$ on the

instrumental parameter ω_0. In the case of TICS, the beam radius is usually calculated from an average of the fit parameters from the 2D spatial autocorrelation functions (15,32). In practice, this value can vary by as much as 30% when determined from cell membranes. This can be due to clusters of fluorescent particles larger than the diffraction limit, which artificially increase the value of the recovered ω_0 by distorting the shape of the spatial ACF. The uncertainty associated with the value of ω_0 therefore decreases the precision of the calculated value of D. The new method we propose decouples the determination of D and $\mathbf{v}$ from ω_0. Similarly, for 3D diffusion studies, no knowledge of the ratio ω_0/ω_z is required (unlike FCS and TICS), because the diffusion constant and this instrumental parameter are completely separable in the reciprocal-space time correlation function.

In traditional ICS or TICS, the number density recovered from the analysis is actually the number of fluorescent particles per beam area (2D). This value is then converted to a more meaningful concentration with units of particles per unit area, using an experimentally determined ω_0. In kICS, the value initially calculated is the average total number of particles in the region of analysis. Converting this value to a density only requires knowledge of the pixel size, a value inherently more precise than ω_0.

More accurate determination of number densities

As shown in Fig. 9 *G*, the density calculated via kICS is less sensitive to the arrangement of the particles in space than its r-space counterpart, ICS. In contrast to ICS and scanning FCS, which assume a random Poisson distribution of particles throughout the region of analysis, the kICS number density is simply a sum over the total number of particles in the entire image. Consequently, kICS is more widely applicable for situations in which the labeled species is present in nonuniform spatial distributions such as gradients. Thus, we believe this will be a useful technique when determining the number densities of heterogeneously distributed proteins. However, even kICS returned highly erroneous values when it was used to analyze the simulated images with narrow dendritic spatial distributions of particles (characterized by discontinuities and large empty spaces). The basic analysis performed here only probes the diagonal spherically symmetric wavevectors. Additional information may be recovered if off-diagonal wavevectors are analyzed.

The basic kICS theory advanced in this work was derived assuming homogeneous, translationally invariant systems. Clearly, these constraints are not satisfied in the dendritic system presented in Fig. 9, and it is not surprising that kICS fails to return accurate number densities in this case. It should be emphasized that kICS will not return reliable transport coefficients if an image series of a sample with similar heterogeneity is analyzed. Ideally, regions of analysis should avoid areas such as the edge of cells, which introduce abrupt changes in the particle distribution. Alternatively, the effect of edges or other significant features could be minimized by filtering their corresponding spatial frequencies in k-space. Fourier filtering the immobile population from single pixel traces also works well for removing large static structures, as has been done in r-space ICS (30).

As with other fluorescence correlation techniques, the number density calculated via kICS is not the absolute number of fluorophores present in the image, but instead the total number of independent fluorescent entities. It cannot be determined if these are monomers, dimers, etc., unless additional experiments are carried out to determine the brightness of a monomeric unit and any fluorophore quenching that may occur when present in multimeric units. As well, the accuracy of a number density measurement using kICS is crucially dependent on a proper subtraction of background intensity counts, as it is with ICS (32).

Differences between kICS, FICS, and FCSTFE

Both FICS (18) and the related technique FCSTFE (17) use an interference pattern generated by two laser beams to selectively excite a single spatial frequency. The total fluorescence emitted from the sample is collected as a function of time, and then autocorrelated. These techniques can be used to determine the structure factor (18) and the bulk diffusion coefficient (20) of fluorescently labeled particles in solution.

While kICS, FICS, and FCSTFE are all based on the theory of Brownian motion (24), several significant differences exist between them. First, FICS and FCSTFE use a custom-built apparatus in which two laser beams interfere at the sample. They also require a lock-in amplifier for detection, and a method to modulate the interference, such as a translation stage or movable grating. In contrast, kICS requires only a commercially available imaging system, such as a scanning laser microscope or TIRF-M.

In addition to the instrumentation differences, in the current work we applied kICS to measure flow velocities of fluorescently labeled particles, as well as the diffusion coefficient. Furthermore, we have shown the transport coefficients extracted via kICS to be insensitive to fluorophore photophysics. This is a significant advantage of the kICS approach due to the ubiquity of photobleaching and/or fluorophore blinking in fluorescence-microscopy-based fluctuation techniques.

Simplified curve fitting

Previous r-space fluorescence correlation techniques such as FCS and TICS fit correlation functions of diffusion to hyperbolic decays, and flow to Gaussian decays. In the nonlinear regression fitting of hyperbolic ACF decays, the value of the returned fit parameters are very sensitive to the weighting used (33). The method we present here allows both types transport to be analyzed without nonlinear curve

fitting. Furthermore, a standard temporal ACF decay that is well fit by a simple diffusive model does not guarantee that there are no contributions from either photobleaching or blinking to the decay (13,25) and (A. Bashir, D. Kolin, B. Hebert, P. Wiseman, unpublished data) which, if present, would lead to significant systematic errors in the diffusion coefficient extracted from the fit. The kICS technique removes this possible source of systematic error as the bleaching or blinking will only affect the intercept.

However, the analysis of samples with more than one population becomes significantly more complicated than with traditional FCS or TICS. With these techniques, the temporal autocorrelation function is fit to an analytical model describing the modes of transport present in the sample. With kICS, the mathematical transformations applied to one-population systems, which are used to generate linear data, can no longer be applied. Instead, a nonlinear fitting routine must be used. As well, the immobile fraction present in a sample cannot be measured as easily as with TICS (28).

Live cell measurement

The cell measurement presented here uses an area detector (i.e., a CCD array), which can offer two significant advantages over the previously used LSM approach. First, most commercially available LSMs have a maximum sampling rate of ~2 Hz, due to the piezoelectric scanning mechanism. The use of a TIRFM in conjunction with a CCD camera allows acquisition rates of at least 30 Hz when imaging GFP transfected cells. Second, even at these higher sampling rates, sensitive CCD cameras offer superior S/N than the typical PMTs, which are standard on commercial LSM systems. Furthermore, this cell measurement illustrates that kICS can measure protein dynamics at expression levels in which individual fluorophores cannot be resolved, a situation that prohibits SPT analysis.

CONCLUSIONS

We presented the theory and application of a novel method to measure the dynamics, number density, and photophysical characteristics of an ensemble of fluorophores. It offers several advantages over previously used techniques; most notably, it can recover accurate dynamics without any knowledge of the fluorophore's blinking or bleaching characteristics, and it does not require the beam waist of the system's PSF to be measured. Possible extensions of this work include: applying it to two-color cross correlation so protein-protein interactions can be quantified in living cells, and developing a variant of the kICS technique that allows for the measurement of shear of macromolecules in biological membranes.

APPENDIX

This appendix explains the derivation leading up to Eq. 16; it closely follows Section 11.5 of Berne and Pecora (21). In obtaining Eq. 16 we have used the simple diffusion model as in the 2D section and have assumed that the system is translationally invariant. That is, the positions of all particles can be transformed $(\mathbf{r}_i) \rightarrow (\mathbf{r}_i + \mathbf{a})$ by an arbitrary vector $\mathbf{a}$. If there are no external forces applied and the system is homogeneous, then this transformation will not perturb the dynamics of the system. Under this transformation, $\tilde{\boldsymbol{\rho}}(\mathbf{k}, t) = \sum_{i=1}^{N} \exp[i\mathbf{k} \cdot \mathbf{r}_i(t)]$ becomes:

$$\tilde{\boldsymbol{\rho}}(\mathbf{k}, t) \rightarrow e^{i\mathbf{k}\cdot\mathbf{a}} \tilde{\boldsymbol{\rho}}(\mathbf{k}, t). \quad (36)$$

Similarly, the Fourier transforms of the density-density correlation functions under this transformation are given by:

$$\langle \tilde{\boldsymbol{\rho}}(\mathbf{k}, t) \tilde{\boldsymbol{\rho}}^*(\mathbf{k}', t+\tau) \rangle = e^{i(\mathbf{k}-\mathbf{k}')\cdot\mathbf{a}} \langle \tilde{\boldsymbol{\rho}}(\mathbf{k}, t) \tilde{\boldsymbol{\rho}}^*(\mathbf{k}', t+\tau) \rangle. \quad (37)$$

This expression must be true for all arbitrarily chosen values of $\mathbf{a}$. Therefore, both sides of Eq. 37 must be zero unless $\mathbf{k} = \mathbf{k}'$. (Strictly speaking, the entire expression is proportional to $(2\pi)^2 \delta(\mathbf{k}_\parallel - \mathbf{k}'_\parallel) = A\Delta_{\mathbf{k}_\parallel, \mathbf{k}'_\parallel}$ in a finite system, where A is the system's area, and Δ is a Kronecker-δ. Because we examine correlations only where $\mathbf{k}_\parallel = \mathbf{k}'_\parallel$, we drop these factors and absorb A into q).

We thank A. F. (''Rick'') Horwitz (University of Virginia) for his generous gift of the α5-integrin/eGFP CHO cell line, and Dr. Daniel Blair (Harvard University) and Dr. Eric Dufresne (Yale University) for their MATLAB particle tracking routines.

D.L.K. was supported by a Natural Sciences and Engineering Research Council (NSERC) scholarship, and previously by funding from Le Fonds Québécois de la Recherche sur la Nature et les Technologies. D.R. acknowledges NSERC. P.W.W. thanks NSERC, the Canadian Institutes for Health Research, and the Canada Foundation for Innovation, for partial support of this work.

REFERENCES

1. Lippincott-Schwartz, J., E. Snapp, and A. Kenworthy. 2001. Studying protein dynamics in living cells. *Nat. Rev. Mol. Cell Bio.* 2:444–456.
2. Schwille, P., J. Korlach, and W. W. Webb. 1999. Fluorescence correlation spectroscopy with single-molecule sensitivity on cell and model membranes. *Cytometry.* 36:176–182.
3. Wiseman, P., J. Squier, M. Ellisman, and K. Wilson. 2000. Two-photon image correlation spectroscopy and image cross-correlation spectroscopy. *J. Microsc.* 200:14–25.
4. Axelrod, D., P. Ravdin, D. E. Koppel, J. Schlessinger, W. W. Webb, E. L. Elson, and T. R. Podleski. 1976. Lateral motion of fluorescently labeled acetylcholine receptors in membranes of developing muscle fibers. *Proc. Natl. Acad. Sci. USA.* 73:4594–4598.
5. Saxton, M. J., and K. Jacobson. 1997. Single-particle tracking: applications to membrane dynamics. *Annu. Rev. Biophys. Biomol. Struct.* 26:373–399.
6. Tsien, R. Y. 1998. The green fluorescent protein. *Annu. Rev. Biochem.* 67:509–544.
7. Dickson, R. M., A. B. Cubitt, R. Y. Tsien, and W. Moerner. 1997. On/off blinking and switching behaviour of single molecules of green fluorescent protein. *Nature.* 388:355–358.
8. Sinnecker, D., P. Voigt, N. Hellwig, and M. Schaefer. 2005. Reversible photobleaching of enhanced green fluorescent proteins. *Biochemistry.* 44:7085–7094.
9. Chan, W. C., and S. Nie. 1998. Quantum dot bioconjugates for ultrasensitive nonisotopic detection. *Science.* 281:2016–2018.
10. Bruchez, M., M. Moronne, P. Gin, S. Weiss, and A. P. Alivisatos. 1998. Semiconductor nanocrystals as fluorescent biological labels. *Science.* 281:2013–2016.

11. Yao, J., D. Larson, H. Vishwasrao, W. Zipfel, and W. Webb. 2005. Blinking and nonradiant dark fraction of water-soluble quantum dots in aqueous solution. *Proc. Natl. Acad. Sci. USA*. 102:14284–14289.
12. Bachir, A., N. Durisic, B. Hebert, P. Grütter, and P. Wiseman. 2006. Image correlation spectroscopy studies of blinking dynamics in semiconductor quantum dots. *Appl. Phys. Lett.* 99:064503.
13. Doose, S., J. M. Tsay, F. Pinaud, and S. Weiss. 2005. Comparison of photophysical and colloidal properties of biocompatible semiconductor nanocrystals using fluorescence correlation spectroscopy. *Anal. Chem.* 77:2235–2242.
14. Heldin, C.-H. 1995. Dimerization of cell surface receptors in signal transduction. *Cell*. 80:213–223.
15. Petersen, N., P. Hoddelius, P. Wiseman, O. Seger, and K. Magnusson. 1993. Quantitation of membrane receptor distributions by image correlation spectroscopy: concept and application. *Biophys. J*. 65:1135–1146.
16. Wiseman, P., and N. Petersen. 1999. Image correlation spectroscopy. ii. Optimization for ultrasensitive detection of preexisting platelet-derived growth factor-beta receptor oligomers on intact cells. *Biophys. J*. 76:963–977.
17. Hattori, M., H. Shimizu, and H. Yokoyama. 1996. Fluorescence correlation spectroscopy with traveling interference fringe excitation. *Rev. Sci. Instrum*. 67:4064–4071.
18. Grassman, T., M. Knowles, and A. Marcus. 2000. Structure and dynamics of fluorescently labeled complex fluids by Fourier imaging correlation spectroscopy. *Phys. Rev. E*. 62:8245–8257.
19. Margineantu, D., R. Capaldi, and A. Marcus. 2000. Dynamics of the mitochrondrial reticulum in live cells using Fourier imaging correlation spectroscopy and digital video microscopy. *Biophys. J*. 79:1833–1849.
20. Hansen, R., X. Zhu, and J. Harris. 1998. Fluorescence correlation spectroscopy with patterned photoexcitation for measuring solution diffusion coefficients of robust fluorophores. *Anal. Chem*. 70:1281–1287.
21. Berne, B. J., and R. Pecora. 2000. Dynamic Light Scattering. Dover Publications, New York.
22. Yeh, Y., and H. Cummins. 1964. Localized fluid flow measurements with an He-Ne laser spectrometer. *Appl. Phys. Lett*. 4:176–178.
23. Cummins, H., N. Knable, and Y. Yeh. 1964. Observation of diffusion broadening of Rayleigh scattered light. *Phys. Rev. Lett*. 12: 150–153.
24. Einstein, A. 1905. On the motion—required by the molecular kinetic theory of heat—of small particles suspended in stationary liquid. *Annalen der Physik*. [in German]. 17:549–560.
25. Kolin, D. L., S. Costantino, and P. W. Wiseman. 2006. Sampling effects, noise, and photobleaching in temporal image correlation spectroscopy. *Biophys. J*. 90:628–639.
26. Miller, D. M. 1984. Reducing transformation bias in curve fitting. *Am. Stat*. 38:124–126.
27. Dean, J. 1999. Lange's Handbook of Chemistry, 15th Ed. J. Dean, editor. McGraw-Hill, New York.
28. Wiseman, P., C. Brown, D. Webb, B. Hebert, N. Johnson, J. Squier, M. Ellisman, and A. Horwitz. 2004. Spatial mapping of integrin interactions and dynamics during cell migration by image correlation microscopy. *J. Cell Sci*. 117:5521–5534.
29. Crocker, J. C., and D. G. Grier. 1996. Methods of digital video microscopy for colloidal studies. *J. Colloid Interface Sci*. 179: 298–310.
30. Hebert, B., S. Costantino, and P. W. Wiseman. 2005. Spatiotemporal image correlation spectroscopy (STICS) theory, verification, and application to protein velocity mapping in living CHO cells. *Biophys. J*. 88:3601–3614.
31. Lichtman, J. W., and J.-A. Conchello. 2005. Fluorescence microscopy. *Nat. Methods*. 2:910–919.
32. Costantino, S., J. W. Comeau, D. L. Kolin, and P. W. Wiseman. 2005. Accuracy and dynamic range of spatial image correlation and cross-correlation spectroscopy. *Biophys. J*. 89:1251–1260.
33. Wohland, T., R. Rigler, and H. Vogel. 2001. The standard deviation in fluorescence correlation spectroscopy. *Biophys. J*. 80:2987–2999.